

MICROSEISMIC EVENT ANALYSIS IN CONJUNCTION WITH STIMULATION TREATMENTS AT THE GEOTHERMAL RESEARCH WELL GTGRSK4/05 IN GROß SCHÖNEBECK/GERMANY

Kwiatek, G., Bohnhoff, M., Dresen, G., Schulze, A., Schulte, T., Zimmermann, G., Huenges, E.

GeoForschungsZentrum
Telegrafenberg
D14473 Potsdam, Germany
e-mail: kwiatek@gfz-potsdam.de

ABSTRACT

The technical feasibility of geothermal power production will be demonstrated in the geothermal research wells Groß Schönebeck using a borehole doublet. This task includes safeguarding the thermal fluid cycle and the optimisation of energy conversion technology at the surface. In order to complete the Enhanced Geothermal System, three massive hydraulic stimulations were performed injecting a total of 13000 m³ of water into the well Gt GrSk 4/05. To monitor injection-induced seismicity during the main injection a combined surface and downhole seismic network was deployed including a downhole seismic sensor at 3800 m depth at only 500 m distance to the injection point.

During the injection period of six days with injection rates of up to 150 l/s and maximum injection pressures of nearly 600 bar a total of 70 events were detected and located. Spectral parameters were calculated and magnitudes were found to cover the range $-1.9 < M < -1.1$. The events show a strong spatial and temporal clustering with a maximum number of 22 events per day. The majority of events occurred towards the end of major stimulation phases indicating a similar behavior as observed at similar treatments in crystalline environments but at smaller level of seismic activity and at lowers magnitudes.

INTRODUCTION

The Groß Schönebeck Research wells GrSk 3/90 and GrSk 4/05 are located north of Berlin, Germany, in the eastern part of the North German Basin, which is characterized by sedimentary deposits of several km thicknesses and no noteworthy recent tectonic activity. Low enthalpy geothermal reservoir rocks are to be found here as siliciclastic sediments and volcanics of the lower Permian at an average depth of about 4000 m and at formation temperatures of up to

150°C. In an earlier phase, the existing well Groß Schönebeck (GrSk 3/90) was used to investigate scenarios of enhancing productivity of thermal fluid recovery from the underground. Subsequently the doublet has been completed with a second well (GrSk 4/05) with a total depth of 4400 m. For the development of a maximum effective pay zone this new well is inclined in the reservoir section with 47°. It was drilled in the direction of the minimum horizontal stress ($\sigma_h=288^\circ$) for optimum hydraulic fracture alignment in relation to the stimulated pre-existing well GrSk 3/90. Hence the orientation of any hydraulically induced fractures will be 18°N, in the direction of the maximum horizontal stress.

In summer 2007 three fracture treatments were performed in well GrSk 4/05: two in the sandstone section (Upper Rotliegend, Dethlingen Formation) and one in the volcanic section (Lower Rotliegend). In the low permeable volcanic rocks a massive cyclic waterfrac treatment in conjunction with a low proppant concentration was performed over a period of 6 days to achieve a long-term productivity and a fracture half length of up to 300 m. Flow rates of up to 150 l/s were realised. A total amount of 13.000 m³ of water was injected here with 24 tons of sand as proppant. The maximum injection pressure was 586 bar. In addition, two gel proppant treatments were carried out in the porous and permeable Upper Rotliegend sandstone formations with injection rates of 66 l/s and 58 l/s, respectively. 500 m³ of crosslinked gel were injected in each of the treatments, at maximum well head pressures of 495 bar and 380 bar respectively, each with a load of about 100 tons high strength proppants. A comprehensive description of the stimulation procedure is given by Zimmermann et al. (2008), this issue.

SEISMIC NETWORK

State-of-the-art monitoring of fluid-injection induced seismicity is a key-issue to characterize geothermal

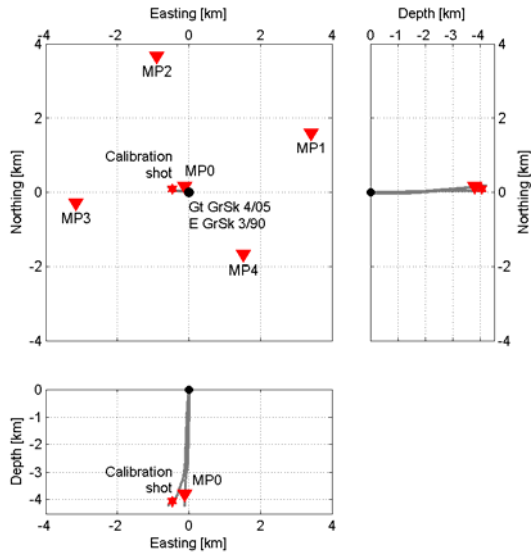


Figure 1. Station distribution of the temporary seismic network at the Groß Schönebeck Geothermal Laboratory during the injection experiment. Seismometer locations are denoted with reverted triangles. The location of calibration shot is indicated by a star.

reservoirs and to quantify the seismic hazard related to large-magnitude events (LME). At Groß Schönebeck the site conditions for a near-surface based seismic network are limited due to the thick sedimentary formations and evaporitic sequences at depth. Both result in significantly decreased signal to noise ratios of seismic waves with distance from the source (see Weber et al., 2005).

To achieve good seismic monitoring conditions during the massive stimulation of the volcanic section we therefore deployed a low-magnitude detection threshold seismic network consisting of seven three-component seismometers including a downhole seismometer operated at 3800 m depth in GrSk 3/90 at only ~500 m distance to the injection point (see Figure 1). The additional six instruments were located at the surface and in shallow (~60 m deep) boreholes framing the surface positions of the deep boreholes. The deep borehole sensor was of type Geospace HS-1 with a natural frequency of 15 Hz and sampling rate of 1000 Hz. Stations located at the surface and in shallow boreholes were equipped with MARK SERCEL L4-3C seismometer (1 Hz) and SENSOR SM6-B geophones (4.5 Hz), respectively, and all sampled at a rate of 200 Hz. The acquisition system was continuously recording between 2nd and 22nd August 2007 framing the massive injection. Data recovery rate of the network was 95%. Regional seismic events from the Legnicko-Glogowski Copper District

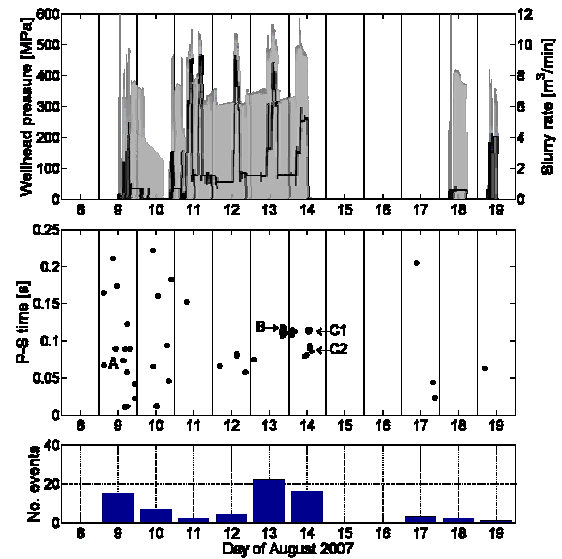


Figure 2. Top: The temporal change of wellhead pressure value (shaded areas) and injection rate (black line) during the injection experiment. Middle: S-P times at the deep borehole sensor. Bottom: Number of induced seismic events per day. The arrows mark the B, C1 and C2 clusters analyzed in this study (see text for details).

in Poland; (8th August 2007, $M_L=3.7$ and 15th August 2007, $M_L=4.3$) served to calibrate the network. Those recordings and a calibration shot that was fired at 4000 m depth in the injection well were used to determine the orientations of the downhole sensors at an accuracy of 15°.

Noise levels at the seismic sensors were sufficient to allow good monitoring conditions. However, during injection the recordings from the deep downhole sensor were contaminated by noise from the water pumps. This noise covered distinct frequency ranges (30-40 Hz, 60 Hz, 110-130 Hz, 200-230 Hz and 300-320 Hz) that partially overlap with the frequency band of expected seismicity. Pumping noise amplitudes were directly related to the injection rate (see Zimmermann et al., 2008, this issue). As a result recording conditions were limited during periods of large injection rates.

INDUCED SEISMICITY

More than 70 seismic events were detected by the downhole seismometer based on a LTA/STA (long-term average/short-term average) detection algorithm supported by an autoregressive AIC picker (e.g. Leonard & Kennett, 1999). The maximum daily event rates were observed on 13th and 14th of August,

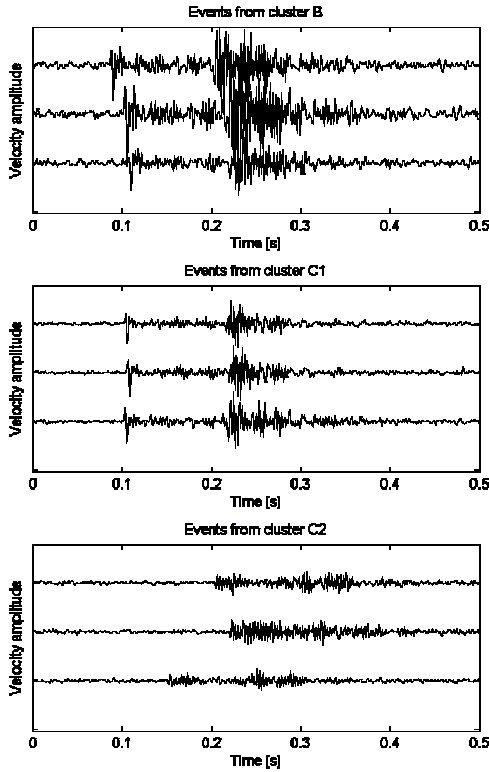


Figure 3. Examples of waveforms recorded at the downhole sensor during the injection experiment. Each panel presents the vertical component for three recorded events from clusters B, C1 and C2, respectively, from top to bottom. Amplitudes are uniformly scaled.

ID	Date Duration	No. events	Well head pressure before/during sequence [Bar]	Injection rate before/during sequence [m ³ /min]
A	Aug 9 120 min	>10	300-400 / 200-400	1-2 / 0
B	Aug 13 90 min	> 20	450-550 / 350	2-8 / 1
C1	Aug 14	6	500-550 / 0	3-5 / 0
C2	120 min	>3		

Table 1. Seismic sequences recorded during the injection experiment.

i.e. towards the end of the injection. The number of events detected per day together with the injection rate and well head pressure is shown in Figure 2. Because of the high frequency content (100-150 Hz) of recorded seismic events compared to the sampling rate, as well as the large source-receiver distances exceeding 5 km, even the strongest induced events were recorded neither by the surface stations, nor by the seismometers in shallow boreholes. This is

explained by the damping of predominantly high frequencies along the ray path in the sedimentary environment as described earlier. As a consequence we focused on recordings at the deep borehole sensor in the following analysis. Most of the seismic events tend to cluster in space and time (sequences A, B and C; see Figure 2). The first sequence A (see Table 1) occurred after the two short injection tests on the 9th of August and lasted for 1.5 hours consisting of >10 events that were hardly detectable even by the downhole seismometer at ~500m hypocentral distance.

The second and most prominent sequence B (Figure 2) was recorded on 13th of August and occurred two hours after the flow rate decreased from 5 m³/min to less than 1 m³/min coinciding with a drop in well-head pressure from 50 to 30 MPa. The seismic sequence lasted for ~1.5 hours and consisted of more than 20 events with clear P and S wave onsets on the borehole sensor. Interestingly, 6 events of this sequence form 3 doublets with 200, 600 and 700 ms time difference between the P-wave onsets, respectively. The S-P time is consistent for all events (114 ms). Sequence C occurred after the end of injection on 14th of August. It was composed of more than 9 events with high signal-to-noise ratios for both P and S arrivals. Sequence C can be divided into two subgroups. The first subgroup (C1) consisted of 6 events with highly similar waveforms and identical S-P times of 112 ms. These events might reflect repeating earthquakes on the same fault patch as observed earlier during fluid-injection experiments (e.g. Baisch and Harjes, 2003) The second subgroup (C2) includes at least 3 events with similar waveforms and S-P time of 91 ms. Three examples of recorded seismic events are shown in Figure 3.

During the gel frac in the more porous and permeable sandstone formations (18th and 19th of August, see Figure 2) the number of observable induced seismic events is even smaller and drops to two events per day.

POLARIZATION ANALYSIS AND HYPOCENTER LOCATION

The S-P times for sequences B and C were generally coherent at 110-117 ms for B and C1 or 91 ms for C2. According to the velocity model for the hypocentral area ($V_p=4.5$ km/s, $V_s=2.6$ km/s) this corresponds to a distance from the downhole sensor of ~700 m and ~550 m, respectively. The picking accuracy for P and S onsets does not exceed three samples (for the noisiest events), corresponding to ± 18 m hypocentral distance. To determine azimuth and incidence angle at the sensor we applied a polarization analysis (e.g. Plesinger et al., 1986) to the three-component recordings and find an accuracy

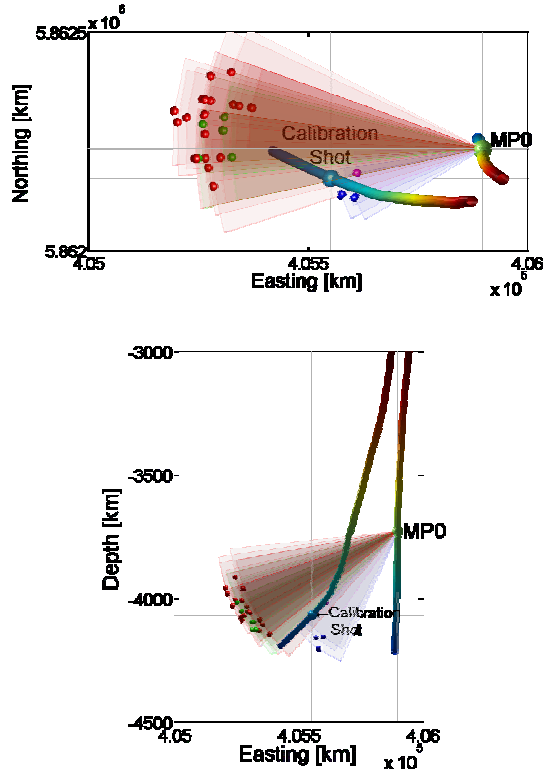


Figure 4. The approximate locations of seismic events considered in this study (red, green and blue points for cluster B, C1 and C2, respectively) after the polarization analysis and correction for seismometer orientation. Shaded areas denote $\pm 10^\circ$ uncertainties in angle estimation.

of 10° between individual events. Considering the accuracy in sensor orientation results in an overall error of 25° for the absolute hypocenter locations. Finally, we were able to locate a total number of 29 induced seismic events all being associated with the sequences B and C (Figure 4).

SPECTRAL ANALYSIS

Using the values of the azimuth and angle of incidence from polarization analysis of P-wave pulse, the three component seismograms were rotated into the local ray coordinate system (R, SV and SH) to perform a spectral analysis. A numerical integration filter was applied to the ground velocity records to obtain the displacement waveforms. The selected parts of P- and S-phases (typically not more than 80ms) were tapered using a 10% von Hann's window, then the FFT was applied to both the ground velocity and displacement waveforms. The correction for instrument response has not been applied due to the much higher frequency content of recorded signals compared to the natural frequency of

the borehole seismometer. The value of attenuation factor is not known for the vicinity of the borehole. However, we examined the influence of frequency-independent Q correction on calculated source parameters and applied the correction using typical values of $Q_p=300$ and $Q_s=150$. On average, the seismic moment is affected by a factor of ~ 1.1 for P and ~ 1.6 for S waves ($M_0^{Q=300}/M_0^{Q=\infty}$). The corner frequency differs by no more than ~ 10 Hz or ~ 20 Hz ($f_c^{Q=300}-f_c^{Q=\infty}$) for P and S waves, respectively. The radiated energy, directly related to energy flux is affected quite strongly by a factor of ~ 1.6 and ~ 4.5 and finally, both static stress drop and apparent stress from S phases are 2.5 times greater after correcting for attenuation.

Spectral parameters were estimated from SH and SV components of selected events from clusters B and C, assuming Ω^{-2} Brune's model (Brune 1970, 1971) and the methodology developed by Andrews (1986). The bandwidth used in this study ranged from 50 to 220Hz. We computed spectral parameters from radial component for clusters C1 and C2, where noise was sufficiently small allowing P-wave waveforms to be used for spectral analysis. In a first stage, we calculated Snoke's integrals (Snoke 1987):

$$J_C = 2 \int |v(f)|^2 df ,$$

$$K_C = 2 \int |u(f)|^2 df ,$$

where C= Radial, SV or SH component and where $v(f)$ and $u(f)$ are the ground velocity and displacement spectra, respectively. Then, the corner frequency f_c as well as the spectral level Ω_C was calculated:

$$f_c = \frac{1}{2\pi} \left(\frac{J_C}{K_C} \right)^{1/2} ,$$

$$\Omega_C = 2 \left(\frac{K_C^3}{J_C} \right)^{1/4} .$$

Finally, we computed the spectral level for S waves from SV and SH components, $\Omega_S = (\Omega_{SV}^2 + \Omega_{SH}^2)^{0.5}$, the S wave corner frequency, $f_s = 0.5(f_{SH} + f_{SV})$ and J integral: $J_S = J_{SH} + J_{SV}$. The seismic moment:

$$M_0 = 4\pi\rho V_C^3 R \Omega_C F_C^{-1} ,$$

where $\rho=2900$ kg/m³ is the medium density, V_C is either P or S wave velocity (in this study we assumed $V_p=4.5$ km/s and $V_s=2.6$ km/s), R is the source-receiver distance calculated from the P-S propagation difference time and F_C is the correction for radiation pattern. In this study, the RMS average radiation coefficients were used (Boore & Boatwright 1984): $F_p = 0.52$ and $F_s = 0.63$ for P and S wave,

Day	HH	MM	SS	Distance	Corner Frequency [Hz]	Seismic Moment [Nm]	Moment Magnitude	Energy [J]	Radius [m]	Stress drop [Pa]	Apparent Stress [Pa]
Cluster B											
13	19	56	8	692	115.9	6.4E+06	-1.5	1.142	4.7	26900	3241
13	20	0	56	675	111.5	1.4E+07	-1.2	4.598	4.9	51849	6024
13	20	1	37	710	124.2	5.8E+06	-1.5	1.118	4.4	30093	3487
13	20	4	14	681	122.1	8.7E+06	-1.4	2.600	4.5	42566	5451
13	20	6	40	705	125.2	9.0E+06	-1.4	2.790	4.4	47367	5675
13	20	11	5	720	114.8	6.4E+06	-1.5	0.971	4.8	25974	2770
13	20	11	49	681	121.1	5.8E+06	-1.5	1.029	4.5	27622	3244
13	20	12	53	708	125.8	2.5E+07	-1.1	22.082	4.3	134174	16063
13	20	14	26	698	122.3	7.4E+06	-1.4	1.769	4.5	36523	4343
13	20	15	55	698	119.1	1.5E+07	-1.2	6.852	4.6	68733	8266
13	20	20	2	702	134.3	1.1E+07	-1.3	5.699	4.1	73555	9194
13	20	23	51	705	139.3	6.1E+06	-1.5	1.821	3.9	44503	5418
13	20	29	55	698	126.4	7.5E+06	-1.4	2.111	4.3	40572	5148
13	20	29	55	696	122.3	7.4E+06	-1.4	1.724	4.5	36376	4256
13	20	42	35	714	121.6	7.0E+06	-1.4	1.502	4.5	33915	3899
13	20	42	35	717	136.4	6.3E+06	-1.5	1.674	4.0	43329	4811
13	20	55	48	742	115.8	4.1E+06	-1.6	0.435	4.7	17088	1940
13	20	55	48	712	125.9	9.7E+06	-1.3	3.213	4.3	52092	6043
13	21	7	59	708	116.9	7.4E+06	-1.4	1.430	4.7	31739	3524
13	21	42	57	702	129.0	6.0E+06	-1.5	1.286	4.2	34892	3876
Cluster C1											
14	12	27	13	696	136.1	8.8E+06	-1.4	3.149	4.0	59435	6550
14	12	27	20	690	120.7	8.4E+06	-1.4	2.068	4.5	39855	4476
14	12	38	11	696	174.1	1.7E+06	-1.9	0.232	3.1	23663	2539
14	12	54	32	696	130.8	4.0E+06	-1.6	0.545	4.2	23963	2498
14	13	7	11	696	119.6	7.5E+06	-1.4	1.595	4.6	34436	3888
14	13	17	36	708	133.1	6.6E+06	-1.5	1.647	4.1	41822	4554
Cluster C2											
14	13	29	36	567	132.1	1.7E+06	-1.8	0.106	4.1	10853	1106
14	13	37	11	573	145.8	3.2E+06	-1.7	0.542	3.7	26820	3072
14	14	33	53	548	140.8	2.6E+06	-1.7	0.281	3.9	19341	1991

Table 2. Source parameters of selected seismic events from clusters B and C, calculated using S waves (see text for a detailed explanation). The values of moment magnitude were computed using a standard relationship (see Hanks & Kanamori, 1979)

respectively. Free-surface as well as the site corrections were not needed due to the downhole location of the sensor (e.g. Gibowicz & Kijko, 1994).

The radiation energy was calculated using the following formula (Boatwright and Fletcher 1984):

$$E_C = 4\pi\rho V_C R^2 J_C F_C^{-2}.$$

Source radius r , apparent stress σ_a and static stress drop $\Delta\sigma$ were determined using the following equations: $r = K_C V_S (2\pi f_C)^{-1}$, $\sigma_a = \rho V_S^2 E / M_0$ and $\Delta\sigma = 7M_0 (16r^3)^{-1}$, where K_C is an averaged correction coefficient according to the quasidynamic circular fault model of Madariaga (1976), where $K_p = 2.01$ and $K_s = 1.32$ when focal mechanisms are not known. These correction coefficients provide more reasonable results in the case of small and induced seismic events (Gibowicz & Kijko, 1994). For the apparent stress we assumed the rigidity equal to ρV_S^2 . It is worth mentioning, that the values of apparent stress and static stress drop are not independent, significantly limiting the investigation of scaling properties of seismic sources (cf. Andrews 1986; Richardson & Jordan, 2002). The calculated source parameters are shown in Table 2.

Figure 5a presents the relationship between radiated energy E_S and E_P calculated from P and S phases for clusters C1 and C2. We included a similar relationship for the seismic moments (Figure 5b) and find that the ratio E_S/E_P ranges from 2.2 to 3.8 for cluster C1 and from 3.4 to 8.0 for cluster C2. This is in disagreement with the typical values of this ratio where the energy radiated in P waves is a small fraction of that in S waves, typically 20-30, as suggested by Boatwright and Fletcher (1984). The observed depletion of S waves energy may be attributed to possible non-double couple source mechanisms (Gibowicz et al., 1990) in case where the induced seismic events represent tensile faulting due to crack opening during the injection experiment. However, neither the radiation pattern, nor possible directivity effects due to the observations performed with a single three-component sensor have been taken into account which may significantly affect the energy calculations. The values of seismic moment (Figure 5b) range from $1.23 \cdot 10^6$ to $1.89 \cdot 10^7$ Nm, corresponding to a range in moment magnitudes from $M_w = -1.9$ to -1.1 following Hanks & Kanamori, (1979). The ratio of M_0^S/M_0^P ranged from 0.4 to 0.7. The corner frequencies calculated from S waves (averaged over SH and SV components) and P

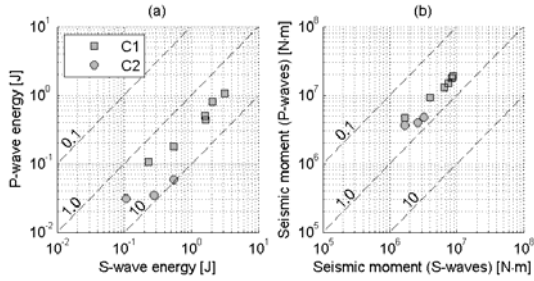


Figure 5. The dependence between source parameters calculated from P and S waves for clusters C1 and C2. The values of constant ES/EP and MOS/MOP ratio are shown as dashed lines.

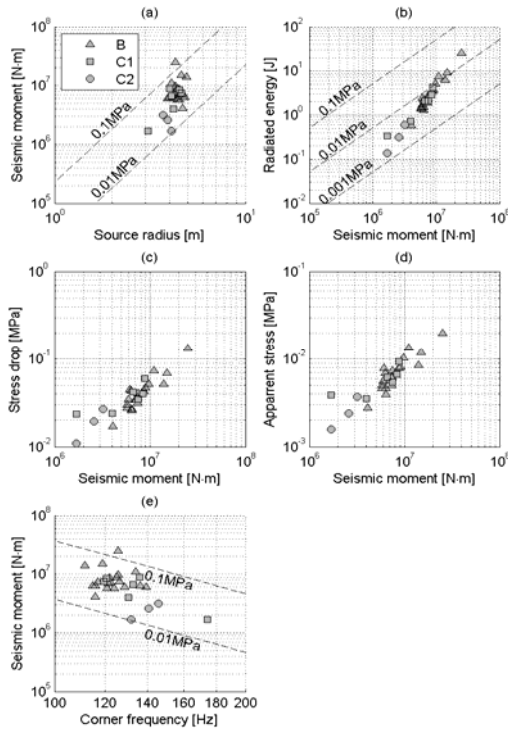


Figure 6. The scaling relationships of source parameters for seismic events from three analyzed clusters B (triangles), C1 (squares) and C2 (circles). The values of constant static stress drop (top-left) and apparent stress (top-right) are shown as dashed lines (see text for details).

waves for clusters C1 and C2 are consistent with f_s/f_p ratio equal to 0.9-1.0. It seems to be an intrinsic source effect, not related to uncorrected attenuation. Interestingly, the corner frequency from SH component is constantly larger than that of SV by on average ~ 25 Hz.

The values of S-wave corner frequency, ranging from 110 to 170 Hz in clusters B, C1 and C2, were subsequently used to calculate the source radii.

The dependence between the seismic moment and source radius is shown in Figure 6a, together with the lines of constant static stress drop equal to 0.01 and 0.01 MPa. The calculation of the source radius, being inversely proportional to corner frequency, is heavily model-dependent. In our case, the values ranged from 3.7 to 4.9 m. The constant stress drop scaling relationship has been reported in many studies (e.g. Brune, 1970, 1971, Gibowicz & Kijko, 1994, Abercrombie 1995). However, we observed a clear dependence between the static stress drop and the seismic moment (see Figure 6c). This indicates relatively slowly increasing source radii with seismic moment, similar to that reported by Jost et al. (1998) for fluid-injection induced seismicity. For the completeness, the dependence between the corner frequency and seismic moment is shown in Figure 6e, showing their weak mutual relationship. The values of static stress drop ranging from 0.01 to 0.1 MPa are rather low in comparison to other studies.

The comparison between the total radiated energy and seismic moment is presented in Figure 6b, together with the lines of constant apparent stress equal to 0.001, 0.01 and 0.1 MPa. The calculated energy is generally smaller than that estimated in previous studies for the same magnitude range (see e.g. Urbancic & Young, 1993, Jost et al., 1998, Oye et al., 2005), even after applying a correction for the significant amount of energy radiated as P-waves (cf. Figure 5a). The underestimation of attenuation does not seem to be the reason and the question remains open whether the influence of rupture directivity and radiation pattern can account for this. The apparent stress ranged from 0.001 to 0.01 MPa and is strongly dependent on seismic moment, as shown in Figure 6d. The scaling of apparent stress with seismic moment is reported in many studies (Abercrombie, 1995, Prejean & Ellsworth, 2001, Kanamori, 2003, Richardson & Jordan, 2002). On the other hand, this scaling relationship is not seen, when all individual data sets are compared over a broad magnitude range (McGarr, 1999; Ide & Beroza, 2001). We conclude that an underestimation of energy for the smallest events or the omission of small events with high energy caused by the limited bandwidth (Richardson & Jordan, 2005) may serve as an explanation.

DISCUSSION AND CONCLUSIONS

We present results of a seismic monitoring campaign during a massive waterfrac experiment at the Groß Schönebeck Geothermal site. A total of 70 events were detected at the deep borehole sensor with clear P and S phase onsets allowing determining spectral parameters. Due to a temporary seismic network that included a seismic sensor in direct vicinity to the injection point at ~ 4 km depth we detected induced seismicity in the magnitude range -

1.9<M<-1.1. None of the induced seismic events was seen at the surface confirming the findings of earlier stimulations at the same site during which no induced seismicity was observed at the surface and in shallow boreholes due to large source-receiver distances.

With a maximum number of 22 events per day the seismicity induced during the frac operation at Groß Schönebeck is very low although injection rates of 150 l/s at maximum injection pressures (at well head) of nearly 600 bar were reached. The majority of events occurred towards the end of major stimulation phases right after maxima in injection rate and formation pressure indicating a similar behavior as observed in crystalline environments such as Soultz-sous-Foret/France and KTB/Germany. However, the study presented here demonstrates that the overall seismic activity is small compared to other sites. This might be explained by the sedimentary environment and limited shear strength compared to crystalline rocks.

REFERENCES

- Baisch, S., M. Bohnhoff, L. Ceranna, Y. Tu, and H.-P. Harjes (2002). Probing the crust to 9-km depth: Fluid injection experiments and induced seismicity at the KTB superdeep drilling hole, Germany. *Bull. Seismol. Soc. Am.* **92** (6), 2369–2380.
- Baisch, S. and H.-P. Harjes (2003). A model for fluid-injection-induced seismicity at the KTB, Germany. *Bull. Seismol. Soc. Am.* **152** (1), 160–170.
- Boatwright, J. and J. Fletcher (1984). The partition of radiated energy between P and S waves. *Bull. Seismol. Soc. Am.* **71**, 361–376.
- Boore, D. and J. Boatwright (1984). Average body-wave correction coefficients. *Bull. Seismol. Soc. Am.* **74**, 1615–1621.
- Brune, J. N. (1970). Tectonic stress and spectra of seismic shear waves from earthquakes. *J. Geophys. Res.* **78**, 4997–5009.
- Brune, J. N. (1971). Correction. *J. Geophys. Res.* **76**, 5002.
- Ellsworth, W. (1995). Characteristic earthquakes and long-term earthquake forecasts: implications of central California seismicity. In F. Cheng and M. Shen (Eds.), *Urban disaster mitigation: The role of science and technology*, pp. 1–14. New York: Elsevier.
- Gibowicz, S. J. and A. Kijko (1994). *An Introduction to Mining Seismology*. San Diego: Academic Press.
- Hanks, T. C. and H. Kanamori (1979). A moment magnitude scale. *J. Geophys. Res.* **84**, 2348–2350.
- Jost, M. L., T. Busselberg, O. Jost, and H.-P. Harjes (1998). Source parameters of injection-induced microearthquakes at the KTB deep drilling site, Germany. *Bull. Seismol. Soc. Am.* **88**, 815–832.
- Leonard, M., and B. L. N. Kennett (1999). Multi-component autoregressive techniques for the analysis of seismograms, *Phys. Earth Planet. Interiors* **113**, 247–264.
- Madariaga, R. (1976). Dynamics of an expanding circular fault. *Bull. Seismol. Soc. Am.* **66**, 639–666.
- Oye, V., H. Bungum, and M. Roth (2005). Source parameters and scaling relations for mining-related seismicity within the pyhasalmi ore mine, Finland. *Bull. Seismol. Soc. Am.* **95** (3), 1011–1026.
- Plesinger, A., M. Hellweg, and D. Seidl (1986). Interactive high-resolution polarization analysis of broadband seismograms. *J. Geophys.* **59**, 129–139.
- Richardson, E. and T. Jordan (2002). Seismicity in deep gold mines of South Africa: implications for tectonic earthquakes. *Bull. Seismol. Soc. Am.* **92**, 1766–1782.
- Urbancic, T. I. and R. P. Young (1993). Space-time variations in source parameters of mining-induced seismic events with $M < 0$. *Bull. Seismol. Soc. Am.* **83**, 378–397.
- Weber, M., Zetsche, F., Ryberg, T., Schulze, A., Spangenberg, E., Huenges, E. (2005). Seismic Detection Limits of Small, Man-Made Reflectors: A Test at a Geothermal Site in Northern Germany. *Bull. Seismol. Soc. Am.* **95**, 1567–1573.
- Zimmermann, G., Reinicke, A., Brandt, W., Blöcher, G., Milsch, H., Holl, H.-G., Moeck, I., Schulte, T., Saadat, A., Huenges, E. (2008), Results of stimulation treatments at the geothermal research wells in Groß Schönebeck/Germany, Proceedings, *Thirty-Third Workshop on Geothermal Reservoir Engineering*, Stanford University, Stanford, California, January 28-30, 2008, SGP-TR-185